

A RADIO RELIC AND A SEARCH FOR THE CENTRAL BLACK HOLE IN THE ABELL 2261 BRIGHTEST CLUSTER GALAXY

SARAH BURKE-SPOLAOR^{1,2,3,4}, KAYHAN GÜLTEKIN⁵, MARC POSTMAN⁶, TOD R. LAUER⁷, JOANNA M. TAYLOR⁶,
T. JOSEPH W. LAZIO⁸, AND LEONIDAS A. MOUSTAKAS⁸

Draft version September 5, 2018

ABSTRACT

We present VLA images and HST/STIS spectra of sources within the center of the brightest cluster galaxy (BCG) in Abell 2261. These observations were obtained to test the hypothesis that its extremely large, flat core reflects the ejection of its supermassive black hole. Spectra of three of the four most luminous “knots” embedded in the core were taken to test whether one may represent stars bound to a displaced massive black hole. The three knots have radial velocity offsets ($|\Delta V| \lesssim 150 \text{ km s}^{-1}$) from the BCG. Knots 2 and 3 show kinematics, colors, and stellar masses consistent with infalling low-mass galaxies or larger stripped cluster members. Large errors in the stellar velocity dispersion of Knot 1, however, mean that we cannot rule out the hypothesis that it hosts a high-mass black hole. A2261-BCG has a compact, relic radio-source offset by 6.5 kpc (projected) from the optical core’s center, but no active radio core that would pinpoint the galaxy’s central black hole to a tight 10 GHz flux limit $< 3.6 \mu\text{Jy}$. Its spectrum and morphology are suggestive of an active galactic nucleus that switched off $> 48 \text{ Myr}$ ago, with an equipartition condition magnetic field of $15 \mu\text{G}$. These observations are still consistent with the hypothesis that the nuclear black hole has been ejected from its core, but the critical task of locating the supermassive black hole or demonstrating that A2261-BCG lacks one remains to be done.

Subject headings: galaxies: nuclei — galaxies: kinematics and dynamics — galaxies: jets

1. IS THE LARGE CORE IN A2261-BCG DUE TO AN EJECTED BLACK HOLE?

It is now understood that supermassive black holes are not only common to the centers of galaxies, but have masses closely tied to the properties of their hosts (Magorrian et al. 1998; Gebhardt et al. 2000; Ferrarese & Merritt 2000). A galaxy and its black hole are formed and evolve together, each influencing the other. The existence of “cores” in the central distribution of stars in luminous elliptical galaxies are hypothesized to be a prominent example of just such a mechanism where the action of the nuclear black hole has shaped the central structure of the galaxy itself. Cores are regions over which the central stellar density distribution breaks as the center of the galaxy is approached, in contrast to the steep envelope density profile of the surrounding galaxy. They were first seen in high resolution images of elliptical galaxies obtained from the ground (Lauer 1985a; Kormendy 1985), and studied extensively in Hubble Space Telescope (HST) images (Ferrarese et al. 1994; Lauer et al. 1995; Laine et al. 2003; Lauer et al. 2005).

Postman et al. (2012) identified A2261-BCG as a galaxy hosting an exceptionally large core. The stellar surface brightness distribution has a cusp radius (the radius at which the local logarithmic slope of the profile is $-1/2$) of $r_\gamma = 3.2 \text{ kpc}$. Its core is thus twice as big as that in the NGC 6166, the BCG with the largest core in the Lauer et al. (2007) compilation, which incorporates the extensive *HST* imaging survey of nearby BCGs of Laine et al. (2003). López-Cruz et al. (2014) subsequently identified an even larger core in A85-BCG, but the core in A2261-BCG remains a strong outlier in comparison to those of nearly all giant elliptical galaxies studied so far.

Postman et al. (2012) further show that the A2261-BCG has a completely flat or even slightly depressed brightness profile interior to the core. Most cores generally have singular, if shallow, cusps interior to the cusp radius (Lauer et al. 1995, 2005). A small number of galaxies have cores with centrally *decreasing* brightness profiles, but they are rare (Lauer et al. 2002, 2005). Postman et al. (2012) hypothesized that both the large core and flat structure could be explained if the nuclear black hole had been ejected from the center of system.

The mass of the expected nuclear black hole (M_\bullet) in A2261-BCG is predicted to be between $5.6 \pm 1.0 \times 10^9 M_\odot$ and approximately $11 \times 10^9 M_\odot$, based on the observed velocity distribution ($\sigma = 387 \text{ km s}^{-1}$, Postman et al.) and the $M_\bullet - \sigma$ relations of Kormendy & Ho (2013) and McConnell et al. (2011), respectively. A somewhat higher upper limit on the mass of the A2261-BCG nuclear black hole can be derived from the fundamental-plane of the black hole activity (Merloni et al. 2003), which estimates M_\bullet from a combination of the core radio luminosity and the nuclear X-ray emission. Hlavacek-Larrondo et al. (2012) use this approach to obtain an estimate of

¹ Center for Gravitational Waves and Cosmology, West Virginia University, Chestnut Ridge Research Building, Morgantown, WV 26505. Email: sarah.spolaor@mail.wvu.edu

² Department of Physics and Astronomy, West Virginia University, Morgantown, WV 26506, USA

³ National Radio Astronomy Observatory, Socorro, New Mexico 87801, USA

⁴ Jansky Fellow for a portion of this work.

⁵ University of Michigan, Department of Astronomy, 301E West Hall, 1085 S. University Ave., Ann Arbor, MI 48109

⁶ Space Telescope Science Institute, 3700 San Martin Drive, Baltimore, MD 21218

⁷ National Optical Astronomy Observatory, P.O. Box 26732, Tucson, AZ 85726

⁸ Jet Propulsion Laboratory, California Institute of Technology, 4800 Oak Grove Dr., Pasadena CA 91106

$M_{\bullet} = 2.0^{+8.0}_{-1.6} \times 10^{10} M_{\odot}$ for A2261-BCG.

Begelman et al. (1980) suggested that the merger of two galaxies, each hosting a central supermassive black hole, would form a binary black hole at the center of the merged system. The binary might then “scour” out a core in the merged system as central stars would gravitationally interact with the binary, drawing orbital energy from it and causing them to be ejected from the center. N-body simulations have demonstrated this phenomenon directly (Ebisuzaki et al. 1991; Makino 1997; Milosavljević & Merritt 2001). Faber et al. (1997) offered strong observational support for this scenario, showing that the most luminous elliptical galaxies nearly always have cores, and are correlated with slow-rotation and “boxy” isophotes in these systems, while less-luminous or rapidly rotating ellipticals rarely have cores. Core formation is thus a natural end-point of “dry mergers” of two progenitor galaxies.

Although there is circumstantial evidence that cores are made by the hardening of a supermassive black hole binary, direct observational proof for the existence of such binaries is still lacking. Other phenomena that come into play during the evolution of the binary may leave their own imprint on the central structure of the hosting galaxies, however, and thus strengthen the case if observed to be directly linked to a black hole pair. Direct observation of SMBH binaries may become possible in coming years by gravitational-wave experiments like pulsar timing arrays (Taylor et al. 2016) or LISA (Flanagan & Hughes 1998).

The terminal hardening of the binary and the subsequent coalescence of the two holes into one may generate a strong jet of gravitational radiation that ejects the coalesced product from the core as well (Redmount & Rees 1989). In either case the sudden removal of the black hole mass would cause the core to rebound and expand in size. If the black hole is not ejected from the galaxy, but remains on a radial orbit that returns it to the center, energy exchange with the stars in the core via dynamical friction may also enlarge the core well beyond its initial size as produced by the hardening of the binary (Boylan-Kolchin et al. 2004; Merritt et al. 2004).

The completely flat core of A2261-BCG strongly resembles the large cores formed by ejection of the central black hole (Gualandris & Merritt 2008). The core of A2261-BCG is also slightly displaced from the photo-center of the surrounding galaxy, suggesting a relatively recent dynamical disturbance, while the rest of the galaxy shows no evidence for recent interaction. Lastly, there are four compact low-luminosity “knots” in close proximity to the core. The ejected black hole is predicted to carry a tightly bound compact “cloak” or hypercompact stellar system (HCSS) of stars with it, potentially similar to these knots (Merritt et al. 2009).

The question that motivates this work is: *Where is the supermassive black hole that should reside in this galaxy?* In §2 we present new (HST) spectroscopic observations of the stellar knots within the core of A2261-BCG to measure their redshifts, stellar velocity dispersions, and to test the possibility that one of them in fact is hosting a wayward black hole. In §3 we present new Jansky Very Large Array (VLA) observations of the radio source in the core of A2261-BCG to test whether active galactic

nucleus activity might mark the black hole. In §4 we discuss how and if the present observations have advanced or refuted the ejected black hole hypothesis.

Throughout this paper, we assume $H_0 = 70 \text{ km s}^{-1} \text{ Mpc}^{-1}$, $\Omega_{\Lambda} = 0.7$, and $\Omega_m = 0.3$. Note also that we adopt two key redshift values throughout this paper. One is the BCG redshift, $z = 0.22331 \pm 0.00024$ (Abazajian et al. 2009), and the other is the mean A2261 cluster redshift, 0.2248 ± 0.0002 (based on over 250 confirmed cluster members). For BCG-related calculations we use the value of 0.22331, while for cluster-wide computations, we use 0.2248. The radial velocity offset of the A2261 BCG relative to the cluster mean redshift is -365 km s^{-1} . This velocity offset is significantly larger than the errors (given above) in either the BCG redshift ($\pm 72 \text{ km s}^{-1}$) or in the mean cluster velocity ($\pm 52 \text{ km s}^{-1}$). The BCG offset from the cluster mean velocity is, however, significantly smaller than the observed velocity dispersion of A2261, which has been measured to be $725^{+75}_{-57} \text{ km s}^{-1}$ (Rines et al. 2010). BCGs are known to exhibit a smaller velocity dispersion about their host cluster mean velocity than that of the average cluster member (Lauer et al. 2014). With the above cosmological parameters, the projected physical scale at the redshift of A2261-BCG is $3.593 \text{ kpc/arcsecond}$.

2. THE PROPERTIES OF THE STELLAR KNOTS IN THE CORE OF A2261-BCG

2.1. Hubble Space Telescope Observations

2.1.1. CLASH Imaging

Photometry and morphology of the A2261 BCG and the 4 knots seen near its core are based on HST data obtained as part of the Cluster Lensing And Supernova survey with Hubble (CLASH) multi-cycle treasury program. The imaging observations were performed between 09-March-2011 and 21-May-2011 in 16 broadband filters from 2250 \AA to $1.6 \mu\text{m}$. The center of Abell 2261 was observed for a total of 20 orbits. Complete details of the HST imaging data acquisition and reduction are given in Postman et al. (2012).

2.1.2. New Spectroscopy

Spectra of knots 1, 2, and 3 were obtained using the Space Telescope Imaging Spectrograph (STIS) from 31-July-2015 to 01-Aug-2015. We used the G750L grating and the $52'' \times 0.5''$ slit. The initial pointing was centered on the brightest knot (knot 3 at R.A. = $17^{\text{h}} 22^{\text{m}} 27^{\text{s}}.14$ and Dec. = $+32^{\circ} 07' 57''.59$ (J2000)). The observations were performed with an ORIENT angle of 130.5 allowing all three knots to be observed simultaneously (Figure 1). We integrated for a total of 8 orbits (total exposure time of 19,100 seconds) and acquired 16 exposures. The 8 orbit integration sequence was executed as two visits, with 300 second acquisition exposures done at the start of orbits #1 and #5 to ensure precise slit alignment. Four small pointing shifts (each $0''.2$ in size and parallel to the long dimension of the slit) were made over the course of 4 orbits to allow for rejection of hot/bad pixels in the dispersion direction. The same shifts were repeated for the second set of 4 orbits.

The STIS data were reduced by performing subtraction of variable herring-bone pattern noise, bias correction and pixel-based charge transfer inefficiency (CTI)

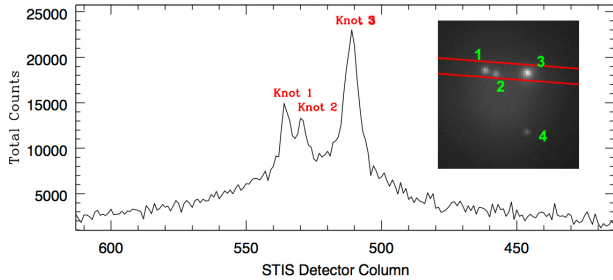


FIG. 1.— The summed spatial profile across 200 rows of the STIS detector demonstrating the acquisition of photons from all three targeted knots. The inset image shows the STIS $52'' \times 0.5''$ slit orientation as red lines, superposed on an HST F775W image of the core of A2261-BCG. The four knots in the A2261 BCG core are numbered by their IDs from Postman et al. (2012). The ORIENT angle for the STIS observations was 130.5° corresponding to a position angle on the sky of 85.5° . This orientation allowed spectra for knots 1, 2, and 3 to be obtained simultaneously. In this image, North is up and West is to the right.

correction on the raw science datasets, then running the remainder of the `calstis` processing steps to produce the final CTI-corrected 2D flat-fielded images. The removal of the herring-bone pattern noise, a known issue with STIS since it resumed operations in 2001 using its Side-2 electronics, was done using the procedures outlined in Jansen et al. (2010). The 2D flat-fielded images were then shifted along the spatial axis using the Pyraf task `sshift` to remove the offsets from the dithers done between each orbit. The individual images were co-added using the `ocrreject` routine, which is designed to detect and remove cosmic rays in STIS CCD data as well as co-add input images. The benefits of using `ocrreject` to combine the data are twofold: (1) an error array is produced which is proportional to the square-root of the output science image, but smaller by a factor that depends upon the square-root of the number of non-rejected input values used to compute the science pixel values and (2) it allowed us to use all 16 exposures to ensure robust CR-rejection. The final 1D spectrum for each knot was extracted using the `x1d` routine which also applies the STIS flux and wavelength calibrations to produce a co-added 1D spectrum in F_λ units of $\text{erg s}^{-1} \text{cm}^{-2} \text{\AA}^{-1}$. The wavelength range of the extracted 1D spectra runs from 5257\AA to 10249\AA , with a dispersion of 4.87\AA per pixel.

The average signal-to-noise ratio (S/N) per resolution element (resel) in the 1000\AA wide range centered on the redshifted NaD doublet feature (centered at 7218\AA at the redshift of $z = 0.2248$ for A2261) for the extracted spectra from knots 1, 2, and 3 is 8.6, 7.7, and 10.7, respectively. The predicted per-resolution-element S/N estimates from the HST exposure calculator were about a factor of 1.8 higher than the achieved values. The large difference between the observed and predicted S/N is primarily due to the significant number of pixels lost to cosmic ray contamination (even with 16 independent exposures) and, to a lesser degree, by residual noise left after the CTI and pattern noise corrections are applied. However, without applying those corrections the observed S/N would have been much worse.

2.2. Central Stellar Velocity Dispersions of the Knots

We fitted the extracted, normalized STIS spectra to estimate the stellar velocity dispersion in the knots. We used pPXF, the penalized pixel fitting code of Cappellari & Emsellem (2004). For each knot spectrum we logarithmically rebinned in wavelength so that it matched that of the MILES library spectra (Vazdekis et al. 2010). To match the spectra, we convolved the higher resolution spectra with a gaussian with variance equal to the difference in variance of our observations and the template spectra. We tried various schemes of binning the spectrum but found they made little difference to our final results. Thus the effective resolution is 250 km s^{-1} . We similarly tried a variety of multiplicative and additive polynomials to account for any residual continuum shape but there was no significant improvement to the fits. Because of the low S/N of our data, we fit only the first two moments (velocity, V , and velocity dispersion, σ) of the line-of-sight velocity distribution relative to the recessional velocity of A2261.

A major concern for our fits to data of low S/N is spurious effects of template mismatch. In order to take this into consideration we used the full MILES library. By using the entire library, we are ensuring that whatever the stellar population of the knots, we have included the proper stellar template. If we had not included the correct stellar template, then at low S/N the penalized pixel fitting method is more likely to find spurious solutions.

A second concern for fits to low S/N is proper accounting of measurement uncertainties in the spectrum. We ran a series of Monte Carlo simulations to create realizations of the spectrum based on the 1D error spectrum after rebinning. The simulated data were fitted for each knot. For each knot spectrum, we ran 1000 realizations and took the median and 68% interval for the V and σ parameters of the fit, weighting them by the reciprocal of the square of the formal fit uncertainties. This weighting scheme ensures that poor fits have less influence on the final results than good fits. All had median results for the velocity dispersion to be very similar to the best-fit results.

The results of our fitting are presented in Table 1. Column 2 in this table is the velocity offset relative to a fiducial redshift of $z = 0.22331$. Column 3 is the derived velocity dispersion. For each knot, the results are expressed as the median values from our Monte Carlo simulations with 68% interval of the parameter distributions for the uncertainties. We plot the 1D spectra with their best fits in Figure 2.

In the spectra for knots 2 and 3, we find no significant evidence for a velocity dispersion larger than that expected for a galaxy with a black hole mass of $\lesssim 6 \times 10^8 M_\odot$. The knot 1 velocity dispersion measurement is highly uncertain, however, and we cannot rule out the hypothesis that knot 1 is hosting the ejected A2261-BCG black hole.

The velocity offsets of the observed knots are significantly less than the velocity dispersions of the A2261-BCG and the A2261 cluster (see §1). The knot velocity offsets are consistent with them being cluster members and they are consistent with potentially being bound to the A2261-BCG as well. However, in §4, we show that the knot velocity offsets are also consistent with the range of predicted initial kick velocities for a SMBH ejection event.

TABLE 1
A2261 KNOT VELOCITY OFFSETS AND DISPERSIONS

Object	Velocity Offset ^a [km s ⁻¹]	Velocity Dispersion ^a [km s ⁻¹]
Knot 1	-74 ⁺⁶⁵ ₋₉₀	175 ⁺¹⁰¹ ₋₅₉
Knot 2	-117 ⁺⁹⁸ ₋₉₇	168 ⁺⁶⁶ ₋₆₃
Knot 3	-58 ⁺⁶² ₋₅₅	209 ⁺³⁹ ₋₄₆

^a The values given are the weighted medians with uncertainties coming from the weighted 16 and 84% of the Monte Carlo distributions. The best fit model spectra used a mixture of stellar templates from the MILES library. Although the modeling procedure can use any of the stars from the full library, in practice only a few templates contribute the most. The non-negligible contributions in decreasing order of relative weights (i) to knot 1 come from G 156-031, HD 187216, and HD 200779; (ii) to knot 1 come from UCAC2 21686546, HD 001326B, 2MASS J15182262+0206397, HD 199799, HD 042474, and HD 183324; and (iii) to knot 3 come from 2MASS J15182262+0206397, UCAC2 21686546, HD 12632, G 171-010, HD 097907, BD+060648, 2MASS J05240938-2433300, HD 042474, and HD 023194.

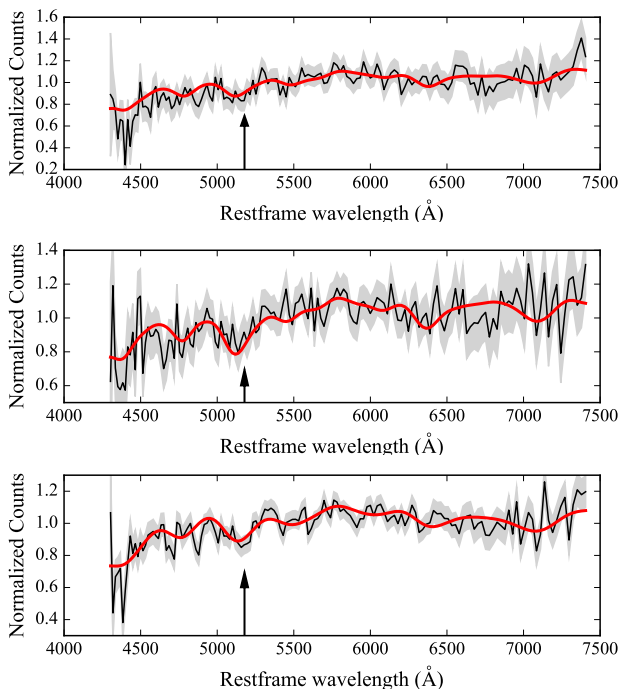


FIG. 2.— The normalized object spectra (black lines) and the 68% confidence intervals on the observed spectrum fluxes (grey shaded areas) are shown for A2261 knots 1, 2, and 3 from top to bottom, respectively. The best fits obtained for each knot are shown as red lines. The arrow indicates the restframe wavelength of the Mgb spectral feature.

2.3. Stellar Population Modeling and Stellar Mass Estimates of the Knots

Stellar masses for the four knots are computed using the `iSEDfit` package (Moustakas et al. 2013). Input photometry for the `iSEDfit` analysis was obtained from 13 broadband images obtained from the CLASH HST Treasury program. All CLASH filters including, and redwards of, F390W were used for our SED fitting. For knots 1, 2, and 4 we used 0".364 (1.31 kpc) diameter apertures and for knot 3 we used a 0".52 (1.87 kpc) diameter aperture. A local background subtraction was performed around each knot in each filter to account for underlying sky and BCG flux contamination. To compute the stellar masses, we generate a grid of 20,000

model spectra using a range of synthetic stellar populations (Bruzual & Charlot 2003), two different initial mass functions [IMF] (Salpeter 1955; Chabrier 2003), and the Calzetti dust extinction law (Calzetti et al. 2000). We then compute the grid of model photometry obtained by convolving the model spectra with HST filter response functions to generate a posterior probability distribution for the parameter space. We adopted a star formation history consisting of an initial burst followed by an exponentially decaying star formation rate (e.g., the BC03 tau model). Table 2 gives the best-fit stellar mass estimates derived for the knots for each of the two assumed initial mass function (IMF) models.

Upper limits on the sizes of the knots are also given in Table 2. The size estimates are the half-width at half-maximum (HWHM) values of the central light distribution of each knot derived from their profiles measured in a deconvolved F814W CLASH image. The image deconvolution was performed by identifying an unsaturated star in the F814W image as our PSF reference and then applying 20 iterations of the Lucy-Richardson deconvolution technique (Richardson 1972; Lucy 1974). The profile for each knot was then measured using the high-resolution `PROFILE` routine (Lauer 1985b) in the `xvista` image processing package. The HWHM values derived for the central light distributions are almost certainly all upper limits. HWHM values in Table 2 are given in both arcseconds and kpc, adopting the projected scale of 3.593 kpc/arcsecond at $z = 0.22331$. All four knots have central light HWHM sizes that are equal to or less than 190 parsecs. We emphasize that these HWHM values are not the same as the effective radius. For example, knot 3 is clearly a fully resolved galaxy but the HWHM of the central light distribution reveals that its nuclear light distribution remains unresolved at *HST*'s angular resolution.

Bonfini & Graham (2016) report the existence of a 5th knot in close proximity to knot 3. We do not model knot 5 as a separate entity. Bonfini & Graham (2016) report that knot 5 is significantly less massive any of the other knots by at least a factor of 10 and is a factor of 150 times less massive than knot 3. The STIS spectrum of knot 3 would have included all the light from knot 5 as well. The S/N of knot 5 would have been far too low for its kinematics to contribute in any way to the kinematic parameters we derived for knot 3.

2.4. Broadband Colors of the Knots

We measured the observed $F475W - F814W$ and $F814W - F160W$ colors for knots 1 through 4 while preparing the input photometry for our stellar mass estimation described in §2.3. The colors of the four knots and that of the BCG (within its central 23.5 kpc) are shown in Figure 3. The colors shown are corrected for local Galactic extinction using the results from Schlegel et al. (1998). Knot 4 is the bluest and Knot 2 the reddest. The four knots are located near the periphery of the red sequence in this color-color space. All four knots are at the red end of the $(F475W - F814W)$ red sequence color distribution although they have $(F814W - F160W)$ colors that are consistent with the bulk of the red sequence galaxies. While we cannot put strong constraints on the age or metallicity of the knots, the SED fitting results suggest that knots 3 and 4 are likely to have subsolar

TABLE 2
BEST FIT STELLAR MASS ESTIMATES AND KNOT CENTRAL SIZE ESTIMATES

Object	Mass in R_m (Salpeter IMF) [$10^{10} M_\odot$]	Mass in R_m (Chabrier IMF) [$10^{10} M_\odot$]	R_m [kpc]	HWHM ^a [arcsec]	HWHM ^b [kpc]
Knot 1	$0.64^{+0.09}_{-0.08}$	$0.37^{+0.05}_{-0.05}$	0.66	≤ 0.047	≤ 0.17
Knot 2	$0.54^{+0.08}_{-0.07}$	$0.31^{+0.05}_{-0.04}$	0.66	≤ 0.043	≤ 0.15
Knot 3	$1.70^{+0.24}_{-0.20}$	$0.98^{+0.15}_{-0.12}$	0.94	≤ 0.053	≤ 0.19
Knot 4	$0.16^{+0.02}_{-0.02}$	$0.09^{+0.01}_{-0.01}$	0.66	≤ 0.041	≤ 0.15

^a The half-width at half-maximum (HWHM) of the central light distribution is derived from the deconvolved F814W CLASH image. See §2.3 for details.

^b Assumes 3.593 kpc/arcsec at $z = 0.22331$, i.e. assumes the knots reside in the BCG core.

metallicity. Specifically, the probability that the stellar populations of knots 3 and 4 are subsolar are 0.93 and 0.91, respectively, for the Salpeter and Chabrier IMF. Our models do not provide any significant constraints on the metallicity of knots 1 and 2.

If the knots are the stripped nuclei of initially larger early-type cluster galaxies then they would be expected to be somewhat redder than the average red sequence cluster member. Elliptical galaxies are observed to have color gradients with the general trend of the stellar population becoming slightly bluer as one moves out to larger radii. Specifically, observed color gradients in ellipticals (Tamura et al. 2000) are $\Delta(F606W - F814W)/\Delta\log(r) \sim -0.06$ in the redshift range $0.2 \lesssim z \lesssim 0.3$. The origin of color gradients in elliptical galaxies appears to be predominantly due to a decrease in the metallicity of the stellar population with increasing radius from the galaxy center. The arrow in Figure 3 shows the direction in which elliptical (F475W-F814W) and (F814W-F160W) colors would change, on average, as one moves from a region corresponding to the size scale of the knots (~ 0.25 kpc) out to a radius of $\sim 2 - 3$ kpc, corresponding to the effective radius of a cluster elliptical. The trend denoted by the arrow corresponds to $\Delta(F475W - F814W) = -0.16$ mag and $\Delta(F814W - F160W) = -0.058$ mag for $\Delta(F606W - F814W)/\Delta\log(r) = -0.06$ and $\Delta\log(r) = 1$. If the knots are the nuclei of stripped early type galaxies then their progenitors are consistent with being red sequence members of Abell 2261.

2.5. *Knots 2 and 3 are likely small cluster galaxies; Knots 1 and 4 remain inconclusive.*

As Tables 1 and 2 suggest, knots 2 and 3 are photometrically and kinematically consistent with the properties of small galaxies. Their velocity dispersions are between 168 and 209 km s⁻¹ and they have stellar masses of 3.1×10^9 and $9.8 \times 10^9 M_\odot$, respectively (using a Chabrier IMF). The velocity dispersions of knots 2 and 3 are inconsistent at the $\gtrsim 2\sigma$ level with systems containing a black hole with mass comparable to that predicted for A2261-BCG, $M_\bullet \gtrsim 5.6 \times 10^9 M_\odot$, which would have yielded an observed stellar velocity dispersion in excess of 330 km s⁻¹ (Kormendy & Ho 2013). Figure 4 shows the predicted range in velocity dispersion for the estimated range in the A2261-BCG black hole mass discussed in section 1. As noted above, the large errors in the velocity dispersion of knot 1 mean that we cannot rule out the

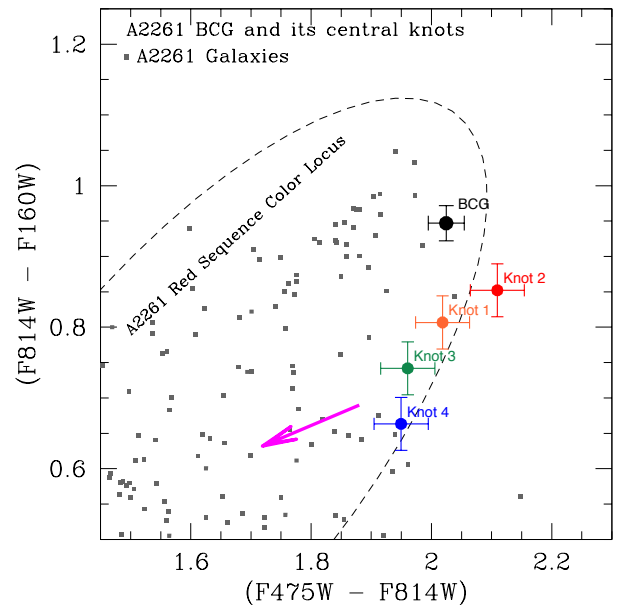


FIG. 3.— The color-color plot of $(F475W - F814W)$ vs. $(F814W - F160W)$ for A2261 knots 1, 2, 3, and 4 as well as that for the A2261-BCG. The error bars are $1-\sigma$ values. Colors for other galaxies in the CLASH observations of A2261 (Conner et al. 2017; private comm.) are shown as grey points. The ellipse identifies the outer boundaries of the color-color parameter space of the A2261 red sequence. The arrow indicates the direction of a typical elliptical galaxy color gradient going from the knot radius of ~ 0.25 kpc to a scale length of 2.5 kpc. The colors of the points for knots 1–4 are simply to guide the eye.

hypothesis that it is hosting a high-mass BH.

3. THE RELIC RADIO SOURCE IN A2261-BCG

3.1. Very Large Array Observations

As reported by Postman et al. (2012), A2261-BCG was detected by the FIRST survey (Becker et al. 1995) as an unresolved 1.4 GHz radio source with a flux of 3.4 mJy, $1''.6$ west of the galaxy’s position; this is just under a factor of two of the galaxy core radius. We thus collected wide-band continuum data from the VLA to obtain:

- Accurate reference frame ties to the available Subaru optical image (Postman et al. 2012) to determine whether the offset position was genuine;
- A resolved image of the radio feature to assess its

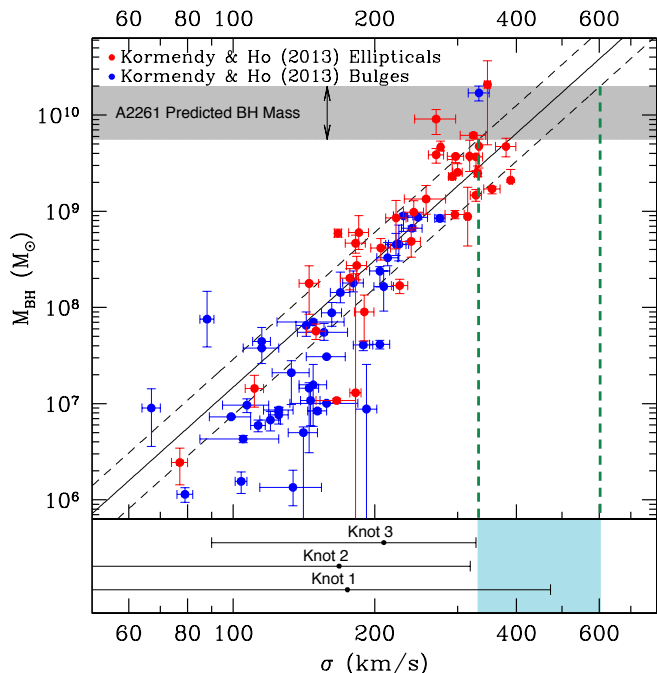


FIG. 4.— Top: The black hole mass, M_{\bullet} , as a function of central stellar velocity dispersion, σ , is shown for the Kormendy & Ho (2013) sample. Their best-fit relation and its 1- σ scatter are shown as black lines. The red and blue points are the measurements for elliptical galaxies and galactic bulges, respectively. The mass range for the nuclear black hole in A2261-BCG is shown as the horizontal gray band. The implied limits on the velocity dispersion from this range of M_{\bullet} values are projected down onto the x-axis by the green dashed lines. Bottom: The observed knot stellar velocity dispersion measurements from this work are shown along with their 95% confidence limits. The blue shaded region shows the expected range in σ for the estimated range in mass for the A2261-BCG black hole.

nature morphologically; and

- An estimate of the jet age through radio spectral aging (e.g. Carilli et al. 1991).

Data were collected under project code VLA/15A-061 in A-configuration in two frequency ranges. The first was 3.976–8.024 GHz (C-band, $f_{\text{avg}} = 5.873$ GHz after flagging, hereafter “6 GHz”), which provided $0''.3$ imaging resolution. The second was 7.976–11.896 GHz (X-band, $f_{\text{avg}} = 9.937$ GHz, hereafter “10 GHz”), which provided $0''.2$ resolution. Both frequency set-ups used standard 2 MHz channel widths and 2 s sampling. Standard primary calibrator 3C286 was used for flux density and bandpass calibration, and source J1735+3616 was used as a phase calibrator. To gain sufficient sensitivity, observations were performed in two epochs and then concatenated to create a single data set per frequency band. Given the extended emission in the source, we do not expect any significant intrinsic variability between the two epochs.

The 6 GHz observations were performed on 11 July 2015, and 13 July 2015, giving a total of 6.27 h on-source time. At 10 GHz, the observations were made on 25 June 2015 and 27 June 2015; 6.70 hours were spent on-source at this frequency. We utilized the standard VLA pipelines to calibrate the data, and performed manual flagging and imaging with the CASA software package. Table 3 provides the resulting image noise, measurement,

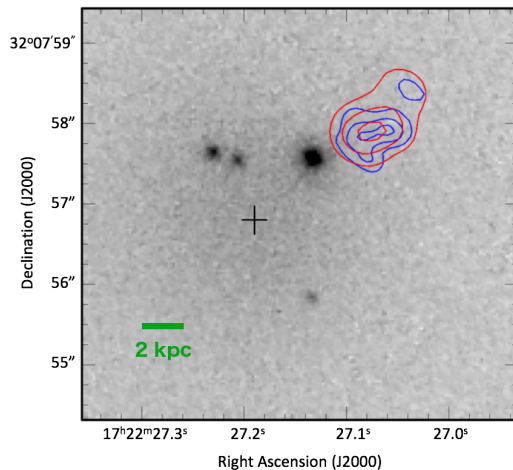


FIG. 5.— The 6 GHz (red) and 10 GHz (blue) contours overlaid on the HST F814W image of the optical knots. Radio contours are at 30, 60, and 90% of the respective image peaks. The photometric centroid of the *core* model of Postman et al. (2012) is marked with a cross.

and beam parameters.

3.2. The radio source is offset from, but related to, A2261-BCG’s core.

FIRST images indicated, to low significance, that there was a radio component offset from the BCG’s core. Our new higher-resolution images (Figure 5) confirm this offset. We find the radio centroid to be $1''.80 \pm 0''.25$ from the photometric center of the optical core.

To verify that an inaccurate radio/optical reference frame tie could not be the cause of the offset, in our data we identified two field sources detected in both our VLA image and the Subaru image (an R-band image from Suprime-cam; Postman et al. 2012). The positions of the optical centroid and the unresolved radio core component of these galaxies, and their radio/optical positional differences, are reported in Table 4. In the same table we show A2261-BCG’s fitted radio position (fitting the X-band data for a single gaussian source), and the core’s peak optical pixel location after the knots have been removed. We thus find the offset of the radio source to be significant and not due to a reference frame error.

We can also assess the probability that this radio source is a projected association and not a genuine one. The galaxy lies in the center of a dense cluster, and so general radio counts will likely underestimate this number. We thus measure the radio source count directly from the A2261-BCG field using an image out to the full width half maximum image at C-band, which has the larger field of view of the two frequencies. The C-band field of view is 0.01 deg^2 . There were three objects in this field with flux densities equal to or larger than the flux density of the A2261-BCG radio source, including the A2261-BCG radio source itself. Thus, the count is $R(\gtrsim 140 \mu\text{Jy}) \simeq 300 \text{ deg}^{-2}$ in this field. The radio offset is 6.5 kpc ($1''.80$), which subtends a circular aperture around the core center of area $3.9 \times 10^{-7} \text{ deg}^2$. A radio source of this flux density had a probability of 1.2×10^{-4} to be in the galaxy core by chance; we are thus confident that the radio detection is related to the core.

One further possibility is that we are seeing a weakly

TABLE 3
VLA IMAGING RESULTS

Band	f_{center} (GHz)	σ (μJy)	Peak (μJy)	Int. (μJy)	Beam size (mas)	Beam P.A. (deg)	Source Size (mas)	Source P.A. (deg)	Linear extent (kpc)
C	5.873	2.1	132.4 ± 6.8	483 ± 31	530×360	68.0	$950 \pm 70 \times 470 \pm 60$	135 ± 5	3.45
X	9.937	1.2	23.4 ± 1.9	158 ± 14	340×220	72.0	$840 \pm 80 \times 490 \pm 60$	126 ± 9	3.05

TABLE 4
ASTROMETRIC VERIFICATION. PARENTHESIS INDICATE ERROR ON LAST DIGIT.

Object	Radio (J2000)		Optical (J2000)		Offset (")
	R.A.	Dec	R.A.	Dec	
Field Spiral	17:22:17.01(2)	+32:09:12.8(5)	17:22:17.016(7)	+32:09:13.1(1)	0.3 ± 0.5
Elliptical galaxy	17:22:26.920(3)	+32:06:36.793(3)	17:22:26.919(7)	+32:06:36.8(1)	0.01 ± 0.15
A2261-BCG radio (10 GHz)/optical core	17:22:27.072(3)	+32:07:57.8(2)	17:22:27.190(7)	+32:07:56.8(1)	1.80 ± 0.25

lensed (magnified) background galaxy. While the source is also not radially elongated, as we might naively expect for a weakly lensed object, this might be due to structural complexity in the lensed galaxy and/or the BCG itself. However, the radio source lies within a nominal Einstein radius for this object ($\sim 8''$ assuming a point mass, $z = 0.3$ of the background galaxy, and $M_{2500} \simeq 10^{14} M_{\odot}$ for the BCG), making significant magnification unlikely. Future work will have to investigate this possibility further using more complex modeling of the mass distribution in the large, flat core in which this radio source resides.

3.3. The radio source is a relic with no presently active core.

The radio luminosity of this source is $\sim 5 \times 10^{23} \text{ W Hz}^{-1}$, as determined from the FIRST flux density. The most compact component at C-band has a brightness temperature of $T_{\text{B}} > 1.4 \times 10^3 \text{ K}$. The emission appears to cover a projected linear extent of around $1 \times 3.5 \text{ kpc}$, with a projected centroid offset of 6.5 kpc from the core. Using our new flux measurements and previous lower-frequency measurements by Hogan (2014), we find a spectral index of $\alpha = -1.5 \pm 0.1$, in agreement with their fit of the lower-frequency data only. Figure 7 shows a resolved two-point spectral index map of our 6 and 10 GHz data across the full extent of the radio emission. Although there is substantial error on the indices in this map (~ 0.5 – 1 on-source), it is clear that there are no flat-spectrum sub-components in the observed emission that could feasibly represent a presently active nuclear black hole.

The spectrum and morphology of this emission are strong evidence that the radio object is in fact relic emission, whose steep slope is indicative of an aged population of synchrotron-emitting electrons (e.g. Scheuer & Williams 1968; Carilli et al. 1991). Relics encompass a range of morphologies and properties, however as argued by Feretti et al. (2012), compact relics without sharp edges that are resident in the cores of galaxies are interpreted either as a fading jet component from a source that is no longer active, or as a “radio phoenix,” which can arise due to compression shocks during a merger that re-energizes plasma from a previously emitting radio jet (e.g. Ensslin et al. 1998). However, the central location of this emission, and the lack of other larger-scale emission directly related to the BCG, appear to imply that

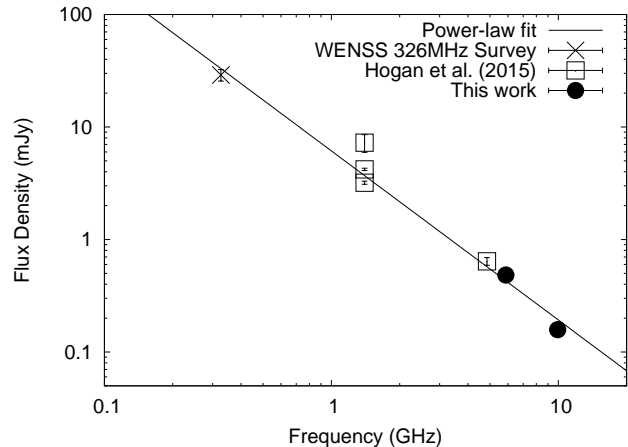


FIG. 6.— The spectral energy distribution of the A2261-BCG radio source. Our measurements indicate a consistency with a single power-law with a steeply declining spectrum. The steep spectral index of this object and the lack of spectrally (or spatially) resolved core component implies that the radio source is in fact no longer active. Note that our WENSS survey data point differs from that of Hogan et al. because for this data point they used the radio source at the center of the Abell 2261 cluster, rather than the BCG itself.

this relic marks an active nucleus shut-off event. We cannot isolate what caused the central object to cease its activity; it could simply have run out of fuel, or it could be a merger- or recoil-induced quenching of the radio emission.

The limited size of the emission is suggestive that either the black hole’s activity was short-lived (such that it had insufficient time to grow to a large radio source), and/or that any radio emission extended beyond the central regions of the galaxy faded more quickly due to lower pressure and magnetic field strength (and thus now only the central regions are visible).

A last, but more tenuous, possibility for the origin of the relic in this core is that it is old emission that originated from the extended active galactic nucleus that exists approximately $2'.5$ northwest of the BCG, in a direction of about 45° from north. Note that this is the object referred to as a “field spiral” in Table 4, as identified by the Subaru image. This plasma may have been re-energized due to sloshing or shocks from ongoing cannibalization in the A2261-BCG core. The other radio object, at J2000 RA, Dec J17:22:17, +32:09:13, has emis-

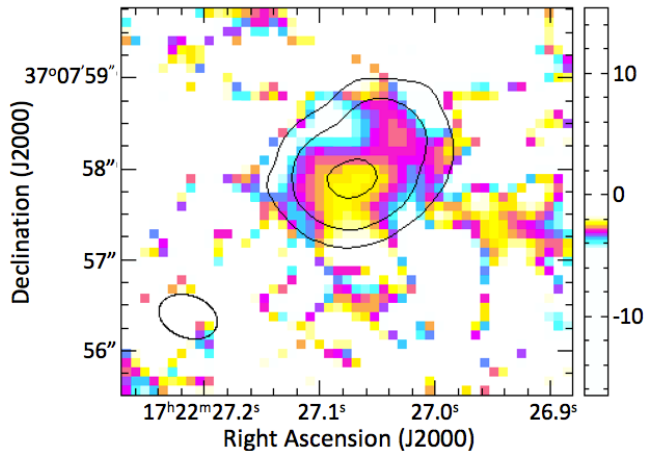


FIG. 7.— A two-point spectral index map of the field based on our 6 and 10 GHz data, where spectral index α is defined as $S \propto f^\alpha$. Contours are shown for the tapered 6 GHz data to give a reference for source placement. The lowest contour is at three times the root-mean-square noise in the 6 GHz image; toward the edges of the object the contours become non-physical. The bulk of the source has a spectral index of around -2 , while its spectral index steepens somewhat towards the north-western spur. These indices are indicative of aging synchrotron emission, implying the source is not currently active. No core emission was detected to the 3σ flux limit of $6.3 \mu\text{Jy}$ and $3.6 \mu\text{Jy}$ in the C- and X-bands, respectively.

sion that extends from its central bright source outwards in a general direction towards the core of A2261-BCG, as shown in the maps of Sommer et al. (2017). The direction of the core of that object in general agrees with the offset direction of the radio source with the A2261-BCG photometric centroid. If one draws a line from the BCG center through its resident relic, it points generally down the barrel of the other galaxy’s axis and through its central bright source. While this is suggestive, it does not imply direct causality.

We also explored whether this object could be explained as a medium-sized symmetric object (MSO), a kiloparsec-scale radio source representing an intermediate stage in the evolution of extragalactic radio sources from parsec scales (compact symmetric objects [CSOs]) to the classical Faranoff-Riley II sources (Fanti et al. 1995; Readhead et al. 1996). This interpretation would favor the presence of an offset SMBH, resident somewhere within the offset location of the radio emission. The principal objection to this explanation is that this source is significantly under-luminous relative to the expectations for MSOs. CSOs and MSOs show well-defined scalings of luminosity and size, with objects having a size scale of order 1 kpc expected to have spectral luminosities of order $10^{27} \text{ W Hz}^{-1}$ at 5 GHz (Fanti et al. 1995; Readhead et al. 1996; Tremblay et al. 2016). By contrast, the spectral luminosity of this source at 5 GHz is approximately $7 \times 10^{22} \text{ W Hz}^{-1}$. While the scatter in this relation is large (~ 1 dex), it is insufficient to accommodate this difference. A secondary objection is that this source is spectrally anomalous relative to most CSOs and MSOs, which tend both to have a flat-spectrum core and only a small fraction of the source with a spectral slope as steep as -1.5 . Even in the regions where spectral indices are steeper than this, these regions are typically at the edges of the source, rather than being the entire source

(Tremblay et al. 2016). Finally, CSOs and MSOs tend to be made up of a set of compact objects rather than dominated by a continuous, resolved component, as this object is.

3.4. How old is the radio relic?

We can place a limit on the age of the radio component in this galaxy using synchrotron aging models, e.g. Harwood et al. (2013). These typically model the broadband radio spectrum with a double power-law, with a break frequency (f_b) above which the aging electrons have a steep spectrum, and below which the spectrum exhibits a more standard ($\alpha \simeq -0.7$) injection value. In these models, f_b and the ambient magnetic field in the radio lobe (B) can be used to estimate the time since last electron acceleration: $t = 1610 B^{-3/2} f_b^{-1/2} \text{ Myr}$, with B in μG , and f_b in GHz (c.f. Pacholczyk 1970; Ensslin et al. 1998).

From Figure 6, there appears to be no clear low-frequency spectral break down to the lowest data point at 326 MHz (Rengelink et al. 1997). Given the steep spectrum across these frequencies that is well-fit to a single power law, we therefore infer that the break frequency is $f_b < 326 \text{ MHz}$. We also require a magnetic field to translate this to a limit on relic age. In the absence of any determinations of the magnetic field in A2261-BCG, Figure 8 shows the inferred range of relic age estimates for break frequencies ranging from 10 MHz to 326 MHz, as a function of magnetic field strength. The implication is that the relic must be very old (>10 ’s of Myr), have an uncharacteristically high magnetic field, or both. The very low spectral break implied for this source implies a magnetic field in the relic on the order of $\gtrsim 2 \mu\text{G}$ if the relic is aged 1 Gyr, and $\gtrsim 15 \mu\text{G}$ for a more typical relic age of 50 Myr.

We can estimate the magnetic field by assuming equipartition between magnetic energy and relativistic particle energy. Following Pacholczyk (1970), and assuming that there is equal energy in heavy particles and a filling factor of 1 (i.e. the magnetic field occupies the whole region rather than in filaments), the minimum value of the total energy is reached when:

$$B_{\min} = (9 c_{12})^{2/7} R^{-6/7} L^{2/7} \quad (1)$$

where R is the source depth, L is the luminosity, and where in CGS units $c_{12} = 1.7 \times 10^8$ is a factor that depends on the radio spectrum and a lower and upper frequency cutoff, assumed here to be 10 MHz and 100 GHz, respectively (e.g. Harris et al. 1993). Note that 10 MHz is a standard choice for a lower cutoff, while the choice of upper frequency cutoff does not greatly effect the results (between choices of 1 GHz and 100 GHz, B_{\min} varies by $<0.5 \mu\text{G}$). For radio relic depth of $\sim 3 \text{ kpc}$, we find the equipartition magnetic field is $\sim 15 \mu\text{G}$. Note that because the equipartition field is most sensitive to the size of the source, and because this radio source is compact when compared to other radio relics, the magnetic field in this object is about one to two orders of magnitude higher than more diffuse radio relics (e.g. Giovannini et al. 1993). This is large, but perhaps unsurprising given the location of this relic in proximity to the core of this BCG.

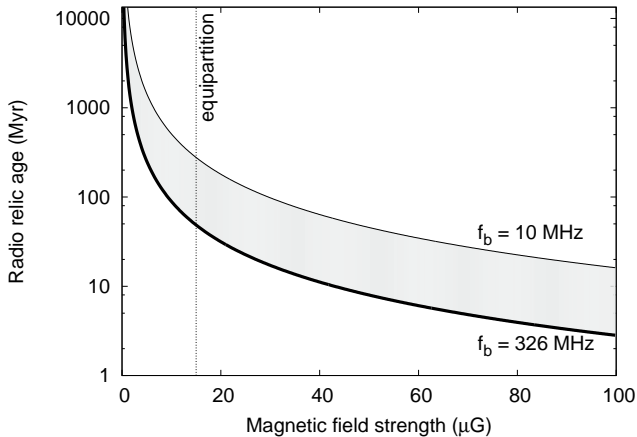


FIG. 8.— Radio relic age as a function of local magnetic field strength. The 326 MHz line represents the largest plausible spectral break frequency based on the observed spectrum. Equipartition sets a lower limit on the source age to > 48 Myr, with an estimated range ~ 50 –200 Myr.

3.5. The jet relic does not mark an optical knot.

It is tempting to trace the jet axis’s alignment back to A2261-BCG’s optical core position or to one of the knots. However, based on the likely age of the jet and mobility of the knots, we conclude that the relative positioning of the radio and optical components cannot be meaningfully interpreted.

4. DISCUSSION

The original hypothesis we set out to address was whether a recoiling SMBH was present in this system, and thus could have helped form the large, photometrically flat, and offset core. We will first address how our new measurements affect this hypothesis.

4.1. Assessment of knots as hypercompact stellar system candidates

The knots were put forward by Postman et al. (2012) as candidates for stellar knots cloaking a recoiling SMBH. Based on the photometric and spectroscopic similarity to the BCG itself, we are now confident that these knots are in fact resident members of the A2261-BCG core. In Section 2.5, we demonstrated that knots 2 and 3 are consistent with being likely cannibalized small galaxies, and given their low velocity dispersions of 168 – 209 km s^{-1} are no longer a candidate HCSS for a roaming SMBH. Thus, we are left with knots 1 and 4 as HCSS candidates, however based strictly on their colors, knots 1 and 4 could feasibly also be interpreted as stripped cluster members. As previously discussed, our large error bar on knot 1 only rules out the HCSS hypothesis at a $\sim 1.5\sigma$ level and thus measurements of higher S/N are still required to rule out the hypothesis confidently.

Based on our new measurements, we can attempt some consistency checks to further investigate knots 1 and 4 as potential HCSS candidates. Merritt et al. (2009) formulated a relationship between the total mass of stars bound to the black hole M_s , black hole mass M_\bullet , host galaxy velocity dispersion σ , and initial kick velocity V_k :

$$\frac{V_k}{1000 \text{ km s}^{-1}} \simeq 0.21 \left(\frac{\sigma}{200 \text{ km s}^{-1}} \right) \left(\frac{M_s}{M_\bullet} \right)^{-2/5}. \quad (2)$$

Through various mass estimate methods, Postman et al.

(2012) found agreement that the central SMBH in A2261-BCG is on the order of $M_\bullet \sim 10^{10} M_\odot$, while its velocity dispersion is $\sigma = 387 \text{ km s}^{-1}$. Using the stellar mass estimates of Table 2 and the above equation, under the hypothesis that knot 1 is a stellar cloak, this formulation implies kick velocities of between 480 – 600 km s^{-1} . For knot 4, we obtain kick velocities in the range 850 – 1100 km s^{-1} assuming the different IMFs.

We would not expect the velocity offset of an observed cloak to exceed this kick velocity; it is likely to be less due to misalignment with line of sight and dampening of the SMBH velocity over time. Knot 1 appears to be well within these values despite the large error on its dynamical measurements. Should future observations permit dynamical assessment of knot 4, if it represents an HCSS we would likewise not expect its velocity offset from the core to exceed the kick velocity.

We can use the HCSS size prediction of Merritt et al. (2009) to note that for kick velocities in the range 480 – 600 km s^{-1} , the HCSS size is predicted to be up to around 200 pc or $0''.05$ in our images, and therefore this range of velocities is consistent with the HWHM for knot 1, ≤ 0.047 , reported earlier. Thus, this comparison demonstrates consistency with an HCSS model, but not conclusive support. For knot 4, velocities in the range 850 – 1100 km s^{-1} predict smaller effective radii of between 30 and 60 pc , or up to $0''.015$.

Finally, the approximate “sloshing timescale” of the A2261-BCG core is $\sim 10^7 \text{ y}$ (Postman et al. 2012). We can thus note that ignoring drag effects and galaxy potential, a recoiling SMBH may have travelled 5 – 6 kpc given the inferred kick velocities for knot 1, and 8.5 – 12 kpc for knot 4. This is consistent with the observed offset of knot 1 from the center of both the core and the photometric center of the galaxy envelope. Note that our support for knot 1 as an HCSS candidate differs from that of Postman et al. (2012) because they lacked knot mass estimates, and thus had assumed $V_k = 1000 \text{ km s}^{-1}$.

We do not have sufficient S/N on our velocity distribution measurements to assess non-gaussianity of the spectral features, as discussed in Merritt et al. (2009).

Thus knot 1, and knot 4 (for which spectroscopy has not yet been performed), remain candidate stellar cloaks in the recoil scenario.

A2261 has two *Chandra* exposures of 10 and 25 ksec (ObsIDs 550 and 5007, respectively), which do not conclusively reveal any accretion onto a SMBH. The X-ray flux in those data is dominated by 0.5 – 2 keV emission from hot cluster gas, showing a cooled core (Bauer et al. 2005). Above 2 keV , there is some emission, possibly a point source consistent with knot 4, though it is too faint to reliably distinguish it from cluster gas emission.

4.2. Assessment of the radio relic in the A2261-BCG core

The age of the relic radio source can potentially be understood as a time-marker for an event related to disturbance of the central SMBH, and thus we are interested in understanding the age and nature of this relic. We limited the timescale of last electron energization in the radio source to $\gtrsim 50 \text{ Myr}$. The existence of a relic in this BCG is interesting in itself and has a number of potential origins, as discussed in Sec. 3.3.

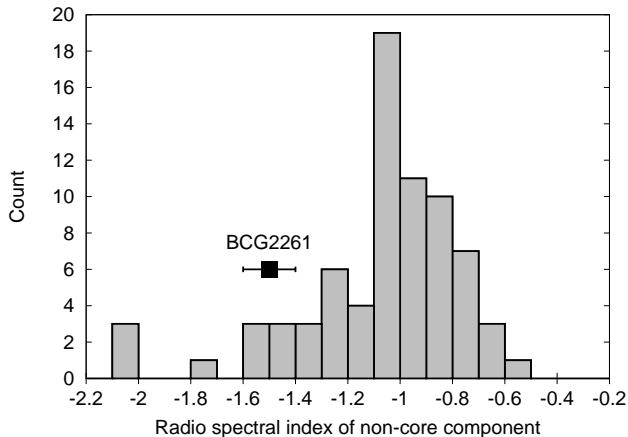


FIG. 9.— The distribution of the spectral index for a subset of the Hogan (2014) BCG sample. Here we show only the $\sim 30\%$ of BCGs in that sample which are similar to A2261-BCG in that only a non-radio-core component has been spectroscopically identified in the BCG. Note that Hogan et al.’s measurement of the A2261-BCG is included in the histogram. Our measurement is indicated separately by a square marker.

To investigate how atypical A2261-BCG’s radio source properties are among BCGs, we compare it with the sample of Hogan et al. (2015), who systematically studied the radio properties of a large sample of BCGs (including A2261-BCG). In comparison with that sample we find that the 1.4 GHz radio luminosity is typical of $\sim 50\%$ of BCGs. We strikingly appear to not detect a distinct core in this object down to a 3σ limit of $< 3.6 \mu\text{Jy}$ at 10 GHz. While the non-detection of a core component in the Hogan (2014) sample was relatively common, their typical upper limit on core emission was on average a factor of >1000 less stringent than our limit. Nevertheless, they found that $\sim 30\%$ of their BCGs had clear spectrally identified radio cores, while 30% consisted of only non-core components (i.e. had upper limits on core emission, as in our case), and 30% were complete radio non-detections; see their Table C.1.

The most unusual thing about the radio relic in A2261-BCG is its central position combined with its small size and steep spectral index. Of the 30% non-core BCGs in the Hogan sample, we show their spectral index distribution in Figure 9. There are only a handful of targets in the sample with spectra comparable or steeper than the central relic in A2261-BCG, and it is likely that given the large selection of BCG of Hogan (2014), there is some contamination from BCG-unrelated cluster relics included in this distribution. The distribution of core-dominated BCGs tend to center on indices closer to $\alpha \sim 0$. Therefore, it seems that the radio spectrum of A2261-BCG lies at the extremity of implied activity and jet ages for BCGs.

4.3. A Stalled Massive Perturber?

The presumption behind our analysis of the A2261-BCG core is that the galaxy hosted a high-mass central BH until perhaps relatively recently. We hypothesized that the BH has been ejected, and might be found in one of the knots or elsewhere in and around the core. Bonfini & Graham (2016) in contrast suggest that the core was generated by the merger of A2261-BCG with a “stalled massive perturber,” which would be the remnant central regions of another galaxy that merged with or was cannibalised by A2261-BCG. The orbital decay of

the perturber “stalls” near the outer regions of a nearly constant-density core (as A2261-BCG has), leaving it to persist as one of the stellar knots.

It appears that the Bonfini & Graham (2016) scenario differs from ours mainly in whether or not A2261-BCG and any of the galaxies that merged with it possess central BHs. As we noted in the introduction, cores are generated in the standard picture as the end point of a “dry merger” of two galaxies that each possess a central BH. Ejection of the central BH in the merger occurs as one outcome when the binary BH formed in the merger coalesces. Bonfini & Graham (2016) do not discuss the role or even the presence of the central BHs in their scenario, and indeed it appears that they are not included in the theoretical models of Goerdt et al. (2010) on which their discussion is based. In short, the Bonfini & Graham (2016) scenario presumes as we do that the core of A2261-BCG presently may not currently harbor a central black hole; however, they implicitly take this as an unexplained initial condition in contrast to our explicit hypothesis that the central BH has been recently ejected.

5. SUMMARY

To summarize, the salient properties of the A2261-BCG are:

- The galaxy has a flat, 3-kpc radius core that contains at least four compact stellar knots (Postman et al. 2012). The knot positions, colors, and kinematics (specifically for knots 1, 2, and 3), imply that the knots are in fact residents of the BCG’s core.
- The core of A2261-BCG is photometrically offset from the center of the surrounding envelope by ~ 700 pc (Postman et al. 2012).
- Knots 2 and 3 are likely small galaxies or larger stripped red sequence galaxies, as evidenced by their colors and by their relatively low internal stellar velocity dispersions and stellar masses.
- Knots 1 and 4 could be dwarf galaxies, stripped cluster members, or stellar shrouds. Our photometric analysis of knot 1 demonstrates that it could be consistent with the Merritt et al. (2009) model for a hypercompact stellar system around a recoiling SMBH, with an implied kick velocity of $V_k = 480 - 600 \text{ km s}^{-1}$, based on our measurements. A more accurate determination of its stellar velocity dispersion is required to test this possibility. The kick velocity estimate for knot 4 is $V_k = 850 - 1100 \text{ km s}^{-1}$.
- The core hosts a radio relic, which appears to represent a past active nucleus that turned off at least 48 Myr ago.

The first two points above provided compelling evidence that there may have been a major merger in the past which led first to a scoured core, and then to a systematic enlargement of this core due to the effects of a SMBH recoil.

With our new information about the radio relic and knots, the recoiling SMBH scenario remains a contender

to explain the above properties of this object. The radio activity is roughly consistent with a core crossing timescale, while knots 1 and 4 could feasibly be consistent with the properties expected from a recoiling HCSS attached to a black hole. However, there is still yet no conclusive indicator as to the precise location of what would be a nomadic $\sim 10^{10}M_{\odot}$ SMBH under this scenario.

A more mundane interpretation of this unusual galaxy's residents is that the knots are cluster members undergoing cannibalization by the BCG, the jet turned off because of a lack of accreting material, and that the core's potentially resident SMBH has no large-scale signatures to mark it. Currently, only circumstantial and theoretical links tie the global interpretation of this object more closely to the recoil hypothesis. Additional observations will be required to vet these hypotheses any further; the detection of large stellar velocity dispersions in knot 1 or 4 would be a strong indicator that either genuinely represents an HCSS. Deeper X-ray observations could also better reveal low-level accretion onto a SMBH in the core. Such an observation would also be sensitive to a bow shock created by a recoiling SMBH and thus

could provide strong positive evidence if it exists.

6. ACKNOWLEDGEMENTS

We thank Thomas Connor for providing early access to his Abell 2261 galaxy photometry catalog and thank Kevin Fogarty for running the `iSEDfit` package on the A2261 knot photometry. This work has been supported in part by NSF award #1458952, and in part by NASA through grants HST-GO-12065.01-A and HST-GO-14046 from the Space Telescope Science Institute, which is operated by the Association of Universities for Research in Astronomy, Inc., under NASA contract NAS 5-26555. The CLASH Multi-Cycle Treasury Program is based on observations made with the NASA/ESA *Hubble Space Telescope*. The National Radio Astronomy Observatory is a facility of the National Science Foundation operated under cooperative agreement by Associated Universities, Inc. Part of this research was carried out at the Jet Propulsion Laboratory, California Institute of Technology, under a contract with the National Aeronautics and Space Administration. We acknowledge a discount by GitHub that assisted with efficient collaborative development of this manuscript. For some calculations in this paper requiring cosmological scaling, we used the online cosmology calculator (Wright 2006).

REFERENCES

- Abazajian, K. N., Adelman-McCarthy, J. K., Agüeros, M. A., et al. 2009, *ApJS*, 182, 543
- Bauer, F. E., Fabian, A. C., Sanders, J. S., Allen, S. W., & Johnstone, R. M. 2005, *MNRAS*, 359, 1481
- Becker, R. H., White, R. L., & Helfand, D. J. 1995, *ApJ*, 450, 559
- Begelman, M. C., Blandford, R. D., & Rees, M. J. 1980, *Nature*, 287, 307
- Bonfini, P., & Graham, A. W. 2016, *ApJ*, 829, 81
- Boylan-Kolchin, M., Ma, C.-P., & Quataert, E. 2004, *ApJ*, 613, L37
- Bruzual, G., & Charlot, S. 2003, *MNRAS*, 344, 1000
- Calzetti, D., Armus, L., Bohlin, R. C., et al. 2000, *ApJ*, 533, 682
- Cappellari, M., & Emsellem, E. 2004, *PASP*, 116, 138
- Carilli, C. L., Perley, R. A., Dreher, J. W., & Leahy, J. P. 1991, *ApJ*, 383, 554
- Chabrier, G. 2003, *PASP*, 115, 763
- Ebisuzaki, T., Makino, J., & Okumura, S. K. 1991, *Nature*, 354, 212
- Ensslin, T. A., Biermann, P. L., Klein, U., & Kohle, S. 1998, *A&A*, 332, 395
- Faber, S. M., Tremaine, S., Ajhar, E. A., et al. 1997, *AJ*, 114, 1771
- Fanti, C., Fanti, R., Dallacasa, D., et al. 1995, *A&A*, 302, 317
- Feretti, L., Giovannini, G., Govoni, F., & Murgia, M. 2012, *A&A Rev.*, 20, 54
- Ferrarese, L., & Merritt, D. 2000, *ApJ*, 539, L9
- Ferrarese, L., van den Bosch, F. C., Ford, H. C., Jaffe, W., & O'Connell, R. W. 1994, *AJ*, 108, 1598
- Flanagan, É. É., & Hughes, S. A. 1998, *Phys. Rev. D*, 57, 4535
- Gebhardt, K., Bender, R., Bower, G., et al. 2000, *ApJ*, 539, L13
- Giovannini, G., Feretti, L., Venturi, T., Kim, K.-T., & Kronberg, P. P. 1993, *ApJ*, 406, 399
- Goerdt, T., Moore, B., Read, J. I., & Stadel, J. 2010, *ApJ*, 725, 1707
- Gualandris, A., & Merritt, D. 2008, *ApJ*, 678, 780
- Harris, D. E., Stern, C. P., Willis, A. G., & Dewdney, P. E. 1993, *AJ*, 105, 769
- Harwood, J. J., Hardcastle, M. J., Croston, J. H., & Goodger, J. L. 2013, *MNRAS*, 435, 3353
- Hlavacek-Larrondo, J., Fabian, A. C., Edge, A. C., & Hogan, M. T. 2012, *MNRAS*, 424, 224
- Hogan, M. T. 2014, PhD thesis, Durham University (UK)
- Hogan, M. T., Edge, A. C., Hlavacek-Larrondo, J., et al. 2015, *MNRAS*, 453, 1201
- Jansen, R. A., Windhorst, R., Kim, H., et al. 2010, in *Hubble after SM4. Preparing JWST*, 50
- Kormendy, J. 1985, *ApJ*, 292, L9
- Kormendy, J., & Ho, L. C. 2013, *ARA&A*, 51, 511
- Laine, S., van der Marel, R. P., Lauer, T. R., et al. 2003, *AJ*, 125, 478
- Lauer, T. R. 1985a, *ApJ*, 292, 104
- . 1985b, *ApJS*, 57, 473
- Lauer, T. R., Postman, M., Strauss, M. A., Graves, G. J., & Chisari, N. E. 2014, *ApJ*, 797, 82
- Lauer, T. R., Ajhar, E. A., Byun, Y.-I., et al. 1995, *AJ*, 110, 2622
- Lauer, T. R., Gebhardt, K., Richstone, D., et al. 2002, *AJ*, 124, 1975
- Lauer, T. R., Faber, S. M., Gebhardt, K., et al. 2005, *AJ*, 129, 2138
- Lauer, T. R., Faber, S. M., Richstone, D., et al. 2007, *ApJ*, 662, 808
- López-Cruz, O., Añorve, C., Birkinshaw, M., et al. 2014, *ApJ*, 795, L31
- Lucy, L. B. 1974, *AJ*, 79, 745
- Magorrian, J., Tremaine, S., Richstone, D., et al. 1998, *AJ*, 115, 2285
- Makino, J. 1997, *ApJ*, 478, 58
- McConnell, N. J., Ma, C.-P., Gebhardt, K., et al. 2011, *Nature*, 480, 215
- Merloni, A., Heinz, S., & di Matteo, T. 2003, *MNRAS*, 345, 1057
- Merritt, D., Milosavljević, M., Favata, M., Hughes, S. A., & Holz, D. E. 2004, *ApJ*, 607, L9
- Merritt, D., Schnittman, J. D., & Komossa, S. 2009, *ApJ*, 699, 1690
- Milosavljević, M., & Merritt, D. 2001, *ApJ*, 563, 34
- Moustakas, J., Coil, A. L., Aird, J., et al. 2013, *ApJ*, 767, 50
- Pacholczyk, A. G. 1970, *Radio astrophysics. Nonthermal processes in galactic and extragalactic sources* (Freeman)
- Postman, M., Lauer, T. R., Donahue, M., et al. 2012, *ApJ*, 756, 159
- Postman et al., M. 2012, *ApJS*, 199, 25
- Readhead, A. C. S., Taylor, G. B., Pearson, T. J., & Wilkinson, P. N. 1996, *ApJ*, 460, 634
- Redmount, I. H., & Rees, M. J. 1989, *Comments on Astrophysics*, 14, 165
- Rengelink, R. B., Tang, Y., de Bruyn, A. G., et al. 1997, *A&AS*, 124, doi:10.1051/aas:1997358

- Richardson, W. H. 1972, *Journal of the Optical Society of America (1917-1983)*, 62, 55
- Rines, K., Geller, M. J., & Diaferio, A. 2010, *ApJ*, 715, L180
- Salpeter, E. E. 1955, *ApJ*, 121, 161
- Scheuer, P. A. G., & Williams, P. J. S. 1968, *ARA&A*, 6, 321
- Schlegel, D. J., Finkbeiner, D. P., & Davis, M. 1998, *ApJ*, 500, 525
- Sommer, M. W., Basu, K., Intema, H., et al. 2017, *MNRAS*, 466, 996
- Tamura, N., Kobayashi, C., Arimoto, N., Kodama, T., & Ohta, K. 2000, *AJ*, 119, 2134
- Taylor, S. R., Vallisneri, M., Ellis, J. A., et al. 2016, *ApJ*, 819, L6
- Tremblay, S. E., Taylor, G. B., Ortiz, A. A., et al. 2016, *MNRAS*, 459, 820
- Vazdekis, A., Sánchez-Blázquez, P., Falcón-Barroso, J., et al. 2010, *MNRAS*, 404, 1639
- Wright, E. L. 2006, *PASP*, 118, 1711